Advances in Nano Research, *Vol. 17, No.2 (2024) 137-147*
https://doi.org/10.12989/anr.2024.17.2.137

Quantum transport of doped rough-edged graphene nanoribbons FET based on TB-NEGF method

K.L. Wong, M.W. Chuan, A. Hamzah, S. Rusli, N.E. Alias, S.M. Sultan, C.S. Lim and M.L.P. Tan*

Faculty of Electrical Engineering, Universiti Teknologi Malaysia, 81310 Skudai, Johor, Malaysia

(*Received December 24, 2020, Revised July 31, 2024, Accepted August 1, 2024*)

Abstract. Graphene nanoribbons (GNRs) are considered a promising alternative to graphene for future nanoelectronic applications. However, GNRs-based device modeling is still at an early stage. This research models the electronic properties of n-doped rough-edged 13-armchair graphene nanoribbons (13-AGNRs) and quantum transport properties of n-doped rough-edged 13-armchair graphene nanoribbon field-effect transistors (13-AGNRFETs) at different doping concentrations. Step-up and edge doping are used to incorporate doping within the nanostructure. The numerical real-space nearest-neighbour tight-binding (NNTB) method constructs the Hamiltonian operator matrix, which computes electronic properties, including the sub-band structure and bandgap. Quantum transport properties are subsequently computed using the self-consistent solution of the two-dimensional Poisson and Schrödinger equations within the non-equilibrium Green's function method. The finite difference method solves the Poisson equation, while the successive over-relaxation method speeds up the convergence process. Performance metrics of the device are then computed. The results show that highly doped, rough-edged 13-AGNRs exhibit a lower bandgap. Moreover, n-doped rough-edged 13-AGNRFETs with a channel of higher doping concentration have better gate control and are less affected by leakage current because they demonstrate a higher current ratio and lower off-current. Furthermore, highly n-doped rough-edged 13-AGNRFETs have better channel control and are less affected by the short channel effect due to the lower value of subthreshold swing and drain-induced barrier lowering. The inclusion of dopants enhances the on-current by introducing more charge carriers in the highly n-doped, rough-edged channel. This research highlights the importance of optimizing doping concentrations for enhancing GNRFET-based device performance, making them viable for applications in nanoelectronics.

Keywords: doping concentration; field-effect transistors; n-doped GNRs; performance metrics; quantum transport; rough-edged; TB-NEGF method; 13-armchair GNRs

1. Introduction

Continuous scaling of the transistor under Moore's law has caused the short-channel effect in a silicon-based field-effect transistor (FET). Thereby, it becomes essential to find an alternative nanomaterial to substitute silicon as the channel of a transistor. The discovery of single layer stable sheet of graphite, known as graphene, has been hailed as one of the alternative materials for the electronic devices in the future (Novoselov *et al*. 2004). However, graphene is a zero bandgap nanomaterial; and hence, it is not suitable to be used as a material to build digital devices for switching application. Narrow strips of graphene or in short, graphene nanoribbons (GNRs) possess similar extraordinary electrical and mechanical properties; and interestingly these nano-ribbons have sizeable bandgaps. Most of the recent research works have been focusing on GNRs (Guseinov *et al*. 2016, Zenkour 2016, Bouadi *et al*. 2018). There are two major edged shapes for GNRs, which are armchair GNRs (AGNRs) and zigzag GNRs (ZGNRs) (Son *et al*. 2006). ZGNRs are always semimetallic since bandgap is absent; hence it is not suitable to be employed as the channel of the transistor, whereas the electronic properties of AGNRs could be changed, depending on their widths. For the widths within *3p* and *3p+1* families, AGNRs are semi-conducting; and otherwise, they are either metallic or semi-metallic. The semiconducting AGNRs channel can be used in FET as bandgap presents, and thus, suitable for digital applications.

In this paper, the electronic and quantum transport properties of pristine GNRs are modelled and simulated under varying widths and lengths. Since the state-of-the-art patterning technique is far from achieving atomic-scale precision, it is almost impossible to fabricate smooth-edged GNRs. Many previous works had concluded that line edge roughness defect would degrade the performance of the nanomaterial and the device. Therefore, dopants are substituted inside the rough-edged channel in this work to improve the performance of the GNRFETs because doping can improve the performance of the device as more majority carriers are introduced. As such, this work is carried out to explore the doped rough-edged GNRFETs with varying doping concentration.

2. Literature review

In 1997, Datta used finite differences method, discretizing spatial coordinates and allowing differential equations

*Corresponding author, Ph.D.,
E-mail: michael@utm.my

ISSN: 2287-237X (Print), 2287-2388 (Online)

converted to their matrix forms to model the mesoscopic systems (Datta 1995). This concept had been widely used to model different types of nanostructure such as carbon nanotube, graphene, GNRs and others. Atomically defined GNRs heterojunctions had successfully been fabricated, and heterojunctions had also been prepared through a late-stage functionalization of chevron GNRs obtained from a single precursor (Nguyen *et al*. 2017). The fabrication of GNRs heterojunctions and heterostructures by combining pristine hydrocarbon precursors with their nitrogen-substituted equivalents had also been reported (Cai *et al*. 2014).

In 2015, Chen *et al*. had synthesized width-modulated AGNRs heterostructures and concluded that bandgap engineering might be achieved by varying the width of covalently bonded segments within the AGNRs (Chen *et al*. 2015). In 2018, Dass *et al*. utilized the tight-binding (TB) method to simulate the electronic properties and bandgap of ideal GNRs (Dass 2018). Moreover, our previous work had modelled the electronic properties of GNRs with line-edge roughness doped with nitrogen and boron (Wong *et al*. 2020c), where we had also compared the electronic properties between the pristine GNRs and doped rough-edged GNRs. The previous research had concluded that the line-edge roughness effect causes bandgap reduction. In addition, it was also found that p-type doping decreases the bandgap further than n-type doping. However, the effect of different doping concentration on the electronic properties of doped rough-edged GNRs had been neglected.

After the discovery of GNRs, extensive studies have also been performed on the device level. In 2007, the real space TB Hamiltonian operator matrix and self-consistent Poisson and Schrödinger equations with open boundary conditions within the non-equilibrium Green's function (NEGF) method were employed to model rough-edged GNR field-effect transistors (GNRFETs) (Fiori and Iannaccone 2007). A subthreshold swing of 64 mV/dec was reported for a GNRFET with a channel width of 1.37 nm and a drain-to-source voltage (V_{DS}) of 0.1 V, indicating good gate control. At V_{DS}=0.5V, the subthreshold swing degraded to 191 mV/dec due to hole-induced barrier lowering (HIBL).

In the same year, the density functional theory-based real-space and NEGF approach was used to investigate the transport properties of AGNRFET with edge substitution of nitrogen or boron dopant (Huang *et al*. 2007). It was demonstrated that that nitrogen-doped GNRFETs exhibited an on-current (I_{ON}) of approximately 1 μA and a minimum off-current (I_{OFF}) of approximately 1.2×10^{-4} μA, resulting in a high on/off current ratio of more than 2000.

In 2010, the Dirac TB approach and self-consistent solution of NEGF and quasi-two-dimensional Poisson solver based on the Dirac equation model were utilized to study the effect of different widths and doping concentrations at the contacts on GNRs tunneling FET (Lam *et al*. 2010). It was found that the device performance varied significantly with ribbon width and doping concentration. For example, a GNR width of 1.2 nm exhibited an on-current (I_{ON}) of 3.29 mA/mm and an off-current (I_{OFF}) of 7.55×10^{-6} mA/mm, resulting in an I_{ON}/I_{OFF} ratio of approximately 4.36×10^{5} and a subthreshold swing (SS) of 43 mV/dec. Increasing the doping concentration at the source improved I_{ON}, while lowering the doping concentration at the drain decreased I_{OFF}.

NEGF formalism combined with first-principles calculation were used to investigate the thermal, electrical and thermoelectric properties in epoxy and hydroxyl groups passivized on ZGNRs' edge (Gao *et al*. 2018). In 2019, four different GNRs-based PN-junctions were designed by doping, and boron-nitrogen doped GNRs-based junctions show little rectification behaviours (Fu *et al*. 2019).

In 2020, our previous work had proposed the real space nearest-neighbour tight-binding (NNTB) method and self-consistent solution of two dimensional Poisson and Schrödinger equation within the NEGF method and successive over-relaxation method to study the quantum transport properties of pristine armchair GNRFETs under varying widths and lengths of the channel (Wong *et al*. 2020d). We reported that for a pristine 13-AGNRFET with a channel length of 5 nm, the subthreshold swing was 141.98 mV/dec, DIBL was 92.45 mV/V, on-current was 7.41×10^{-7}A, off-current was 2.42×10^{-9} A, resulting in an on/off current ratio of 306, and a threshold voltage of 0.26 V. Our previous research had also been extended further by comparing the quantum transport properties of armchair GNRFETs with metal contact between the pristine and doped rough-edged channel at varying channel widths (Wong *et al*. 2020b).

Meanwhile, Baildya *et al*. modelled and simulated a p-n junction device made of AGNRs incorporating boron/ nitrogen doping as well as defects via first-principle calculations based on density functional theory and NEGF approach, where they summarised that doping and defects could lower bandgap compared to pristine GNRs, with nitrogen doping, leading to the smallest bandgap and the highest current when compared with boron doping (Baildya *et al*. 2020).

In 2020, the use of TVS via Lauritsen-Millikan (LM) and Fowler-Nordheim (FN) plots was discussed to identify resonance and saturation points in electronic devices (Santos *et al*. 2020). These methods, along with rectification rate analysis, could provide additional insights into the electronic properties of GNRFET devices by analyzing asymmetry and enhancing understanding of doped GNRs. The influence of hydrogenation, width, and strain effects in Me-graphene devices, highlighting significant modifications in electronic properties, was explored (Sampaio-Silva *et al*. 2022). The electronic transport properties of armchair graphene nanoribbons (AGNRs) within 3p-1, 3p, and 3p+1 families were examined. The study found that doping with boron nitride can improve electron transport for both zigzag and armchair conformations, with elastic transport making the main contribution to current and conductance (Sampaio-Silva *et al*. 2020).

Recent studies have noted the importance of considering various scattering mechanisms and strain effects on the performance of FETs. For example, phonon scattering can significantly influence the electronic transport properties, as demonstrated in studies involving MoS2 FETs. It was found that the ballistic current is reduced by 43.7% for a channel length of 10 nm and 31.8% for a channel length of 6 nm due to phonon scattering. The current reduction was 40.9% at

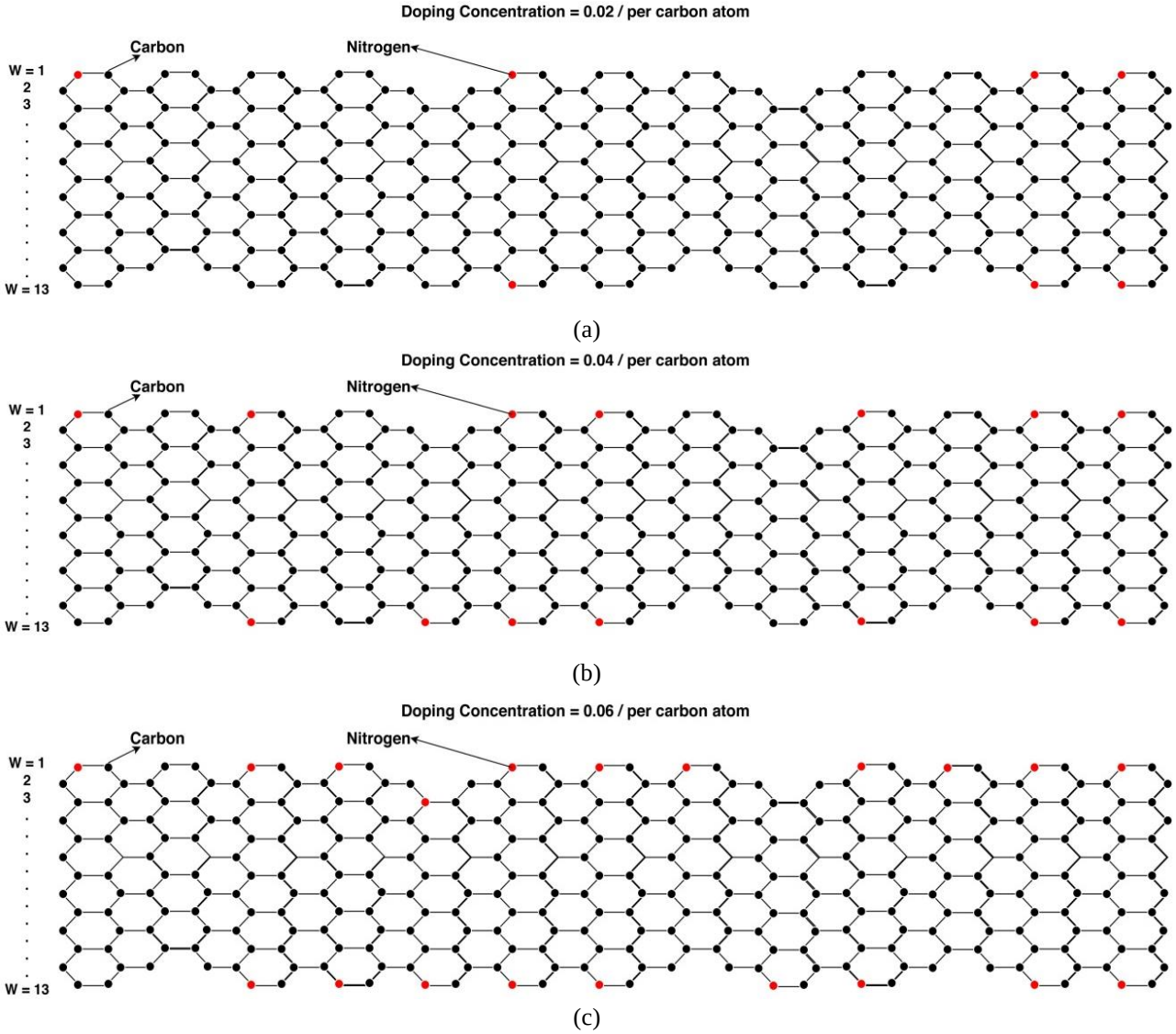

Fig. 1 Atomic structure of doped rough-edged 13-AGNRs with a doping concentration of (a) 0.02, (b) 0.04 and (c) 0.06 per carbon atom. Red dots represent nitrogen dopants, while black dots represent carbon atoms.

200 K and 45.9% at 500 K, with the current at 500 K being 76.4% higher than at 200 K (Chin *et al*. 2023). While this work does not consider phonon scattering and strain effects, these factors are worth investigating in future studies to further understand their impact on the performance of GNRFETs

The versatility of the NEGF method in handling various lattice potentials, including bilayer graphene, demonstrates its capability in studying quantum transport properties. This adaptability enables a precise description of electronic characteristics, as evidenced by a recent study on AB-stacked bilayer graphene. The study quantified the dispersion relation, DOS, and transmission coefficients for zigzag and armchair variants. It revealed a bandgap of approximately 0.25 eV for zigzag bilayer graphene. Significant differences in the transmission spectra were observed based on the stacking configuration, providing valuable insights into their transport properties (Poobalan *et al*. 2024).

Limitations and weaknesses from previous research define the scope of this work. Therefore, this work employs the numerical real space NNTB method to model the electronic properties of n-doped rough-edged 13-AGNRs at different doping concentration such as 0.02, 0.04 and 0.06 per carbon atom. The electronic properties including the sub-band structure and bandgap, are simulated from the Hamiltonian operator matrix of n-doped rough-edged 13-AGNRs. Besides that, this work also simulates the quantum transport properties of n-doped rough-edged 13-AGNRFETs at different doping concentration via the self-consistent solution of two-dimensional Poisson and Schrödinger equation within the NEGF method and successive over-relaxation method. The outputs of the quantum transport properties include the total density of state (DOS) of the device, transmission coefficient and various current-voltage characteristics curve. Next, the performance metrics of the devices are computed and compared among devices of different channel doping concentrations, namely the

subthreshold swing (SS), drain-induced barrier lowering (DIBL), on-current, off-current, on/off current ratio, and threshold voltage.

3. Research methodology

In this research, the numerical real space NNTB method is utilized to construct the Hamiltonian operator matrix for n-doped rough-edged 13-AGNRs and 13-AGNRFETs. Fig. 1 shows the atomic structure of n-doped rough-edged 13-AGNRs with the doping concentrations of 0.02, 0.04 and 0.06 per carbon atom. The positions of the dopants at each concentration are indicated, where red dots represent nitrogen dopants and black dots represent carbon atoms. The simulated 13-AGNRs have a length of 5 nm, equivalent to 13 unit cells. This channel length was selected to ensure clear observation of quantum confinement effects while maintaining computational efficiency. This choice aligns with industry trends towards shorter channel lengths for enhanced performance and power efficiency (Oldiges *et al*. 2020).

Dopant locations are randomly selected inside the nanostructure, based on the rules of step-up and edge doping approach. Since step-up doping is employed, we divide the channel into three regions which are near the source contact, central and near the drain contact. The dopants in each region are increased from near-source region to central and finally near-drain region. 7 nitrogen dopants are substituted for 0.02 per carbon atom doping concentration; 14 nitrogen dopants are substituted for 0.04 per carbon atom doping concentration, and 21 nitrogen dopants are substituted for 0.06 per carbon atom doping concentration. In order to avoid the effect of dopants location, the edge doping technique is employed where only the edges of AGNRs. As a result, the location of dopants could be fixed at the edge as the doping concentration increases. The line edge roughness defect is defined via the exponential auto-correlation method, as discussed in previous research (Wong *et al*. 2020b). In this work, the width and length of AGNRs are fixed; thus the simulated electronic and transport properties are not affected by the dimensional variations.

The general structure of the Hamiltonian operator matrix for 13-AGNRs is computed based on the numerical real space NNTB method, as shown in Eq. (1). The step-by-step derivation of the Hamiltonian operator matrix had been discussed in our previous work (Wong *et al*. 2019a, b, 2020a).

$$H = \begin{bmatrix} \alpha_A & \beta_{AB} & 0 & 0 & 0 & 0 \\ \beta_{BA} & \alpha_B & \beta_{BC} & 0 & 0 & 0 \\ 0 & \circ & \circ & \circ & 0 & 0 \\ 0 & 0 & \circ & \circ & \circ & 0 \\ 0 & 0 & 0 & \beta_{LK} & \alpha_L & \beta_{LM} \\ 0 & 0 & 0 & 0 & \beta_{ML} & \alpha_M \end{bmatrix} \quad (1)$$

where α is the alpha matrix defines the interaction between atoms inside the unit cell and β is the beta matrix defines the interaction between unit cells. The row and column dimension of the Hamiltonian operator matrix is similar to the total number of unit cells inside the GNRs. The similar method is used to define the Hamiltonian operator matrix of the source and drain contacts. Then, the sub-band structure of the n-doped rough-edged 13-AGNRs is simulated via Eq. (2).

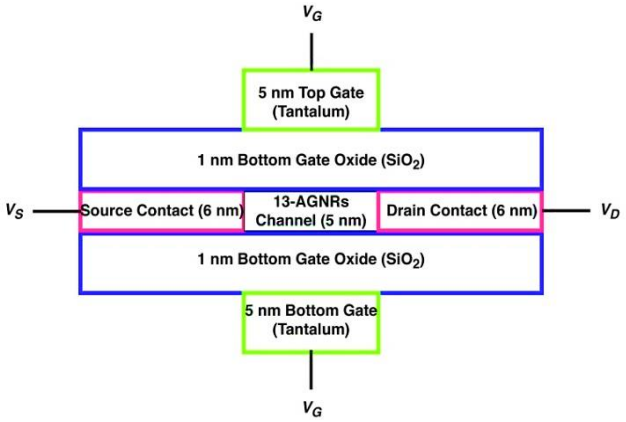

Fig. 2 Two-dimensional general structure of simulated 13-AGNRFETs

$$E = \beta e^{-ika} + \alpha + \beta e^{+ika} \quad (2)$$

In Eq. (2), k is the wave vector, and a or ka denotes the lattice constant or the product of the wave vector and the lattice constant, respectively. The simulated n-doped rough-edged 13-AGNRs are subsequently employed as the channel for 13-AGNRFETs, with connections to metallic zigzag-edged GNR contacts at the drain and source ends. The general structure and Hamiltonian construction of these armchair and zigzag-edged GNR contacts have been thoroughly discussed in our previous research, and thus will not be elaborated upon here. The detailed definitions and values of the alpha and beta matrices can also be found in our prior work (Wong *et al*. 2020b). Fig. 2 shows the two-dimensional general structure of simulated 13-AGNRFETs, which is made of double-gated structure with the 1 nm thick silicon dioxide layers as the gate oxide.

The dielectric constant for silicon dioxide is 3.9. The length of the gate contact is identical to the length of the channel while the length of the drain and source contacts is always 1 nm longer than the length of the channel. Tantalum metal is utilized as the material of gate contact.

The source and drain contacts in our study are composed of zigzag graphene nanoribbons (ZGNRs) with a length of 6 nm. For the device with ZGNR contacts, the source contact is built up by AGNRs arranged in a shifting down arrangement, whereas the drain contact is arranged in a shifting up arrangement to form zigzag-edged [111]. As a result, the width of the ZGNR contact is always larger than the width of the channel by one. For a channel width of 13-AGNRs, the ZGNR contact width is 14 atoms wide. Each unit cell of the 14-ZGNR consists of 28 carbon atoms. Given a length of 6 nm, which corresponds to approximately 14 unit cells (assuming a unit cell length of 0.43 nm), the total number of atoms in the ZGNR would be 392 carbon atom.

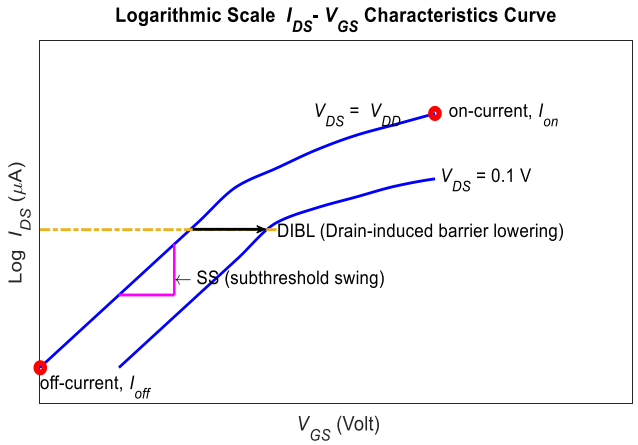

Fig. 3 Example of the logarithm of drain-source current versus gate-source voltage curve on a semilogarithmic scale. V_{DD} is the power supply voltage.

The two-dimensional Poisson equation is solved self-consistently within the NEGF, and the successive over-relaxation method is used to speed-up the convergence process. Eq. (3) illustrates the two-dimensional Poisson equation used in this research (Owlia *et al*. 2017, Shamloo *et al*. 2020).

$$\frac{1}{[2hz^2+2hx^2]}(hz^2[U_{SCF}(x-1,z)+U_{SCF}(x+1,z)]+ \\ \dots\ hx^2[U_{SCF}(x,z-1)+U_{SCF}(x,z+1)]+ \\ \dots\ \frac{qhx^2hz^2\rho(x,z)}{\varepsilon_0\varepsilon_r}=U_{SCF}(x,z) \tag{3}$$

Here, $\rho(x,z)$ is the net charge density distribution counting the doping density, ε_r is the dielectric constant of the silicon dioxide, ε_0 is the permittivity of free space, h_x is the grid spacing in the x-direction, h_z is the grid spacing in the z-direction and U_{SCF} is the self-consistent potential. Different boundary conditions are employed when the finite difference method is utilized to solve the two-dimensional Poisson equation. For instances, Dirichlet boundary condition is imposed at the grid points, which is the boundary between the gate contact and the silicon dioxide while Neumann boundary condition is imposed at the grid points on the other boundaries. Eq. (4) demonstrates the net charge density distribution, $\rho(x,z)$ computation (Khorshidsavar *et al*. 2018).

$$\rho(x,z)=p-n+N_D^+-N_A^+ \tag{4}$$

where p, n, N_D^+ *and* N_A^+ are the holes concentrations, electron concentrations, donor concentrations and acceptor concentrations, respectively. For instance, in a GNR segment with 1000 carbon atoms, a doping concentration of 0.02 per carbon atom means 20 nitrogen atoms ($N_D^+ = 0.02 \times 1000$). These nitrogen atoms act as donors, increasing the electron concentration (nn) and enabling us to study the impact of this doping level on the electronic properties and quantum transport characteristics of the 13-AGNRFETs.After the convergence of self-consistent potential, the total DOS of the device can be calculated through Eq. (5).

$$DOS(E)=\frac{1}{\pi}Im[Trace[G_F]] \tag{5}$$

where G_F is the retarded Green's function as shown in Eq. (6) (Nazari *et al*. 2015, 2016).

$$G_F=G^{retarded}=[(E+i\eta)*I-H-U_{SCF}-\Sigma_S \\ -\Sigma_D]^{-1} \tag{6}$$

where E, η, I, Σ_S and Σ_D are the energy, an infinitesimal positive number, the identity matrix, self-energy matrix of the source contact and self-energy of the drain contact, respectively. The transmission coefficient of the device can be computed through Eq. (7) (Shamloo *et al*. 2017, 2020), given as

$$T(E)=Trace[\Gamma_S G_F\,\Gamma_D G^+] \tag{7}$$

where G^+ is the advanced Green's function, which is the Hermitian conjugate of the retarded Green's function, G_F, and Γ_S and Γ_D is the coupling between the channel and source contact as well as coupling between the channel and drain contact.

Following that, the current can be computed via the Landauer's current equation (Khan *et al*. 2014), expressed as

$$I=\frac{2q}{h}\int_{-\infty}^{\infty}dE\{f(E,U_S)-f(E,U_D)\}T(E) \tag{8}$$

where q is the electronic charge, h is Planck's constant, $f(E,U_s)$ is Fermi functions of the source contact and $f(E,U_D)$ is Fermi functions of the drain contact (Bahrami and Shahhoseini 2017). After computation of the current-voltage characteristics curve, performance metrics of the simulated device can be calculated, including the SS and DIBL as presented in Eq. (9) and Eq. (10) as

$$SS=\frac{\Delta V_{GS}}{\Delta \log I_{DS}}, \tag{9}$$

$$DIBL=\frac{\Delta V_{TH}}{V_{DD}-0.1} \tag{10}$$

where ΔV_{GS} is the difference in the gate-source voltage in mV, $\Delta log10\ I_{DS}$ is the difference in the drain-source current on a logarithmic scale, V_{DD} is the power supply voltage, 0.1 V is the lowest drain-source voltage at the linear region and ΔV_{TH} is the difference in the threshold voltage. Moreover, the on/off current ratio can be calculated as the division between the on-state current, I_{ON} and off-state current, I_{OFF}, expressed as

$$Current\ ratio=\frac{I_{ON}}{I_{OFF}} \tag{11}$$

where on-state current is the maximum current flowing through the device in on-state while the off-state current is the minimum current flowing through the device in off-state when the drain-source voltage is equal to the power supply voltage (Tan *et al*. 2012, Chin *et al*. 2014). Fig. 3 illustrates the computation of the device performance metrics from the semi-logarithmic plot of drain-source current versus gate-source voltage curve.

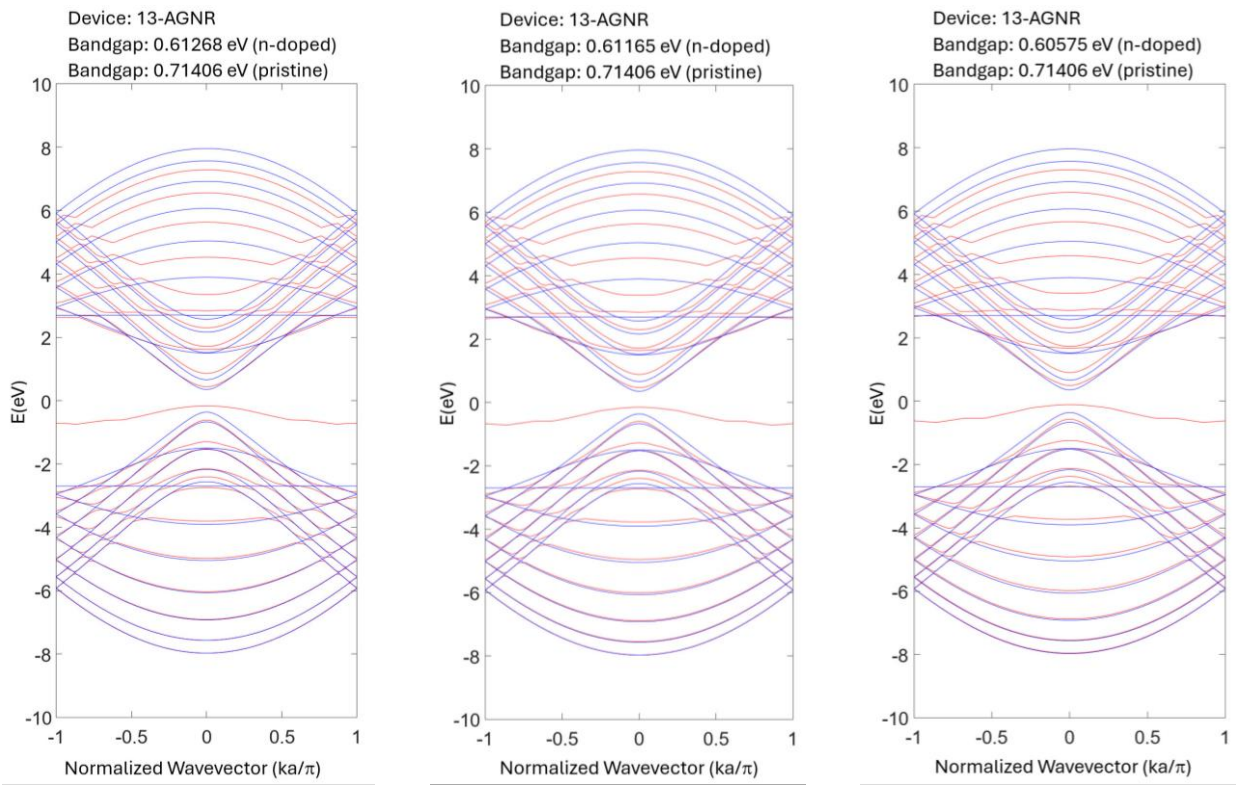

(a) (b) (c)

Fig. 4 Sub-band structure of n-doped rough-edged 13-AGNRs at 5 nm length for doping concentration of (a) 0.02, (b) 0.04 and (c) 0.06 per carbon atom. The blue line indicates the sub-band structure for pristine 13-AGNRs while the red line indicates the sub-band structure for n-doped rough-edged 13-AGNRs

4. Results and discussion

Fig. 4 presents the sub-band structure of n-doped rough-edged 13-AGNRs at 5 nm length for doping concentration of 0.02, 0.04 and 0.06 per carbon atom. The 13-AGNR channel contains a total of 350 atoms, with the doping concentrations corresponding to 7, 14, and 21 nitrogen atoms, respectively. The blue line indicates the sub-band structure for pristine 13-AGNRs while the red line indicates the sub-band structure for n-doped rough-edged 13-AGNRs. In addition, the bandgap is compared between pristine and non-pristine 13-AGNRs. In Fig. 4, the first "*Bandgap"* shown in sub-band structure plot shows the bandgap of the n-doped rough-edged 13-AGNRs while the second "*Bandgap"* shown in sub-band structure plot shows the bandgap of the pristine 13-AGNRs. From the figure, we found that the total number of sub-band is reduced from 26 of pristine 13-AGNRs to 24 of n-doped rough-edged 13-AGNRs. Different doping concentration will affect the bandgap of the n-doped rough-edged 13-AGNRS because the bandgap value reduces when the doping concentration increases. For example, the bandgap of n-doped rough-edged 13-AGNRs with 0.02 per carbon atom doping concentration is 0.613 eV while the bandgap of n-doped rough-edged 13-AGNRs with 0.06 per carbon atom doping concentration is 0.606 eV. Increasing the doping concentration of n-doped rough-edged 13-AGNRs at 300% will reduce the bandgap by about 1.14 %. The maximum and minimum energy of the sub-band structure is almost remaining the same when the doping concentration is increasing.

Fig. 5 demonstrates the total DOS of the device versus energy curve for 13-AGNRFETs with the channel of doping concentration at 0.02, 0.04 and 0.06 per carbon atom which are represented by green, red and blue lines, respectively at gate-to-source voltage of 0.1 V and drain-to-source voltage of 0.5 V. It is observed that varying the channel doping concentration in 13-AGNRFETs has minimal impact on the total DOS of the system. This is evidenced by the fact that all three colored lines overlap at the same position and exhibit identical minimum and maximum energy values. Since the channel is n-doped, the peak at 2.7 eV is higher than the peak at -2.7 eV. Besides that, Fig. 6 illustrates the graph of the transmission coefficient versus energy curve for 13-AGNRFETs with the channel of doping concentration at 0.02, 0.04 and 0.06 per carbon atom which are represented by green, red and blue lines, respectively at 0.1 V of gate-to-source voltage and 0.5 V of drain-to-source voltage. Similar to the total DOS of device plot, the peak above energy level of 0 eV is always higher than the peak below the energy level of 0 eV since the device is n-doped. However, it is observed that the variation of the channel doping concentration for 13-AGNRFETs has a more apparent impact on the transmission coefficient plot, although the impact is not obvious.

From the maximum value of the transmission coefficient, we can notice that the channel of the device with the highest doping concentration has the highest value of transmission

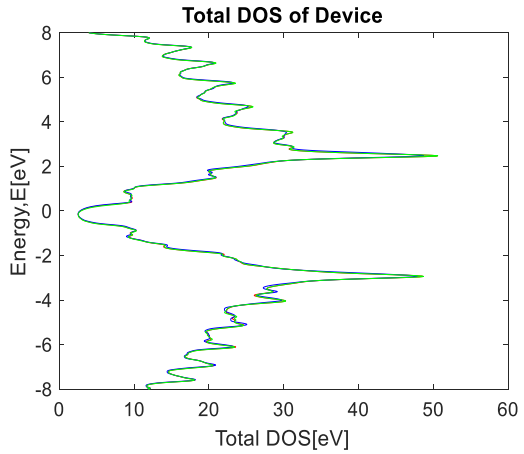

Fig. 5 Total DOS of device versus energy for 13-AGNRFETs with channel of different doping concentration at (a) 0.02 (green), (b) 0.04 (red) and (c) 0.06 (blue) per carbon atom

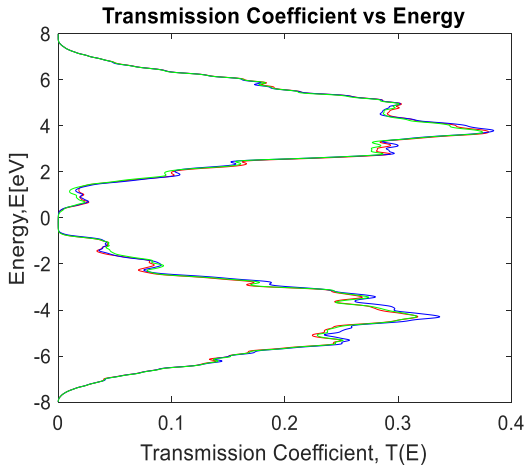

Fig. 6 Transmission coefficient versus energy for 13-AGNRFETs with channel of different doping concentration at (a) 0.02 (green), (b) 0.04 (red) and (c) 0.06 (blue) per carbon atom

coefficient while the channel of the device with lowest doping concentration has the lowest value of transmission coefficient. However, the difference is not drastic. The transmission plot is shown in Fig. 6, where the 13-AGNRFET is biased at a gate-source voltage of 0.1 V. As the gate voltage, V_G increases, the transmission coefficient curve will be shifted downwards, resulting in more conducting region (or mobile charge carriers) that is associated with the current conduction; and thus increasing the value of the drain current during the current computation via the Landauer's current equation.

Fig. 7 presents the drain-source current, I_{DS} versus drain-source voltage, V_{DS} and drain-source current, I_{DS} versus gate voltage, V_G on a semi-logarithmic scale for n-doped rough-edged 13-AGNRFETs at a doping concentration of 0.02, 0.04 and 0.06 per carbon atom at gate voltage and drain-source voltage ranging from 0 V to 1 V with 0.1 V gap. Moreover, the drain-source current, I_{DS} versus gate voltage, V_G for n-doped rough-edged 13-AGNRFETs at a doping concentration of 0.02, 0.04 and 0.06 per carbon atom is shown in Fig. 8 with gate voltage and drain-source voltage ranging from 0 V to 1 V with 0.1 V steps.

The drain-source current, I_{DS} versus gate voltage, V_G on a semi-logarithmic scale for n-doped rough-edged 13-AGNRFETs with a doping concentration of 0.02, 0.04 and 0.06 per carbon atom is illustrated in Fig. 8. The performance metrics of n-doped rough-edged 13-AGNRFETs at lengths of 5 nm with various doping concentrations are summarized in Table 1. From the drain-source current, I_{DS} versus drain-source voltage, V_{DS} curve, we found that the n-doped rough-edged 13-AGNRFETs exhibit strong saturation behaviour and not affected by varying doping concentration. The difference in channel doping concentration only affects the value of saturation current where the saturation current increases from 0.563 μA to 0.731 μA when the doping concentration triples from 0.02 per carbon atom to 0.06 per carbon atom. The subthreshold swing and DIBL of the n-doped rough-edged 13-AGNRFETs are decreases when the channel doping concentration increases. For instances, increasing the doping concentration from 0.02 per carbon atom to 0.04 per carbon atom has reduced the subthreshold swing from 161.48 mV/dec to 139.44 mV/dec and DIBL from 81.73 mV/V to 79.7 mV/V. The decrease in the subthreshold swing is about 13.65% while the reduction in DIBL is about 2.48%. When the doping concentration is increased further to 0.06 per carbon atom, the subthreshold swing and DIBL is further improved to lower values: 139.44 mV/dec and 77.28 mV/V, respectively. Therefore, we can conclude that the device with higher doping concentration at the channel has better channel control and less affected by the short-channel effect.

Besides that, the on-current is increased while off-current is decreased under higher channel doping concentration in the 13-AGNRFETs. The on-current increased from 0.563 μA to 0.731 μA while the off-current is decreased from 1.08 nA to 0.908 nA when the doping concentration of the channel for 13-AGNRFETs increases from 0.02 per carbon atom to 0.06 per carbon atom. The increase in on-current is about 29.8% while the decrease in off-current is about 13.93%; hence the highly doped device is less affected by leakage current effect. Since the on/off current ratio is directly proportional to on-current but inversely proportional to off-current, the on/off current ratio for the n-doped rough-edged device is increased under higher channel doping concentration. For example, the on/off current ratio is increased from 521.30 to 739.50 when the doping concentration of channel increases from 0.02 per carbon atom to 0.04 per carbon atom. When the doping concentration is increased further to 0.06 per carbon atom, the on/off current ratio reaches 805.07. Therefore, we can summarise that device with higher channel doping concentration has better gate control. However, the threshold voltage, which is the minimum voltage to create a conducting path between the source and drain contacts, has increased when the doping concentration of the channel for 13-AGNRFETs increases. For instances, the threshold voltage increases from 0.18 V to 0.3 V when the channel doping concentration increases from 0.02 per carbon atom to 0.06 per carbon atom.

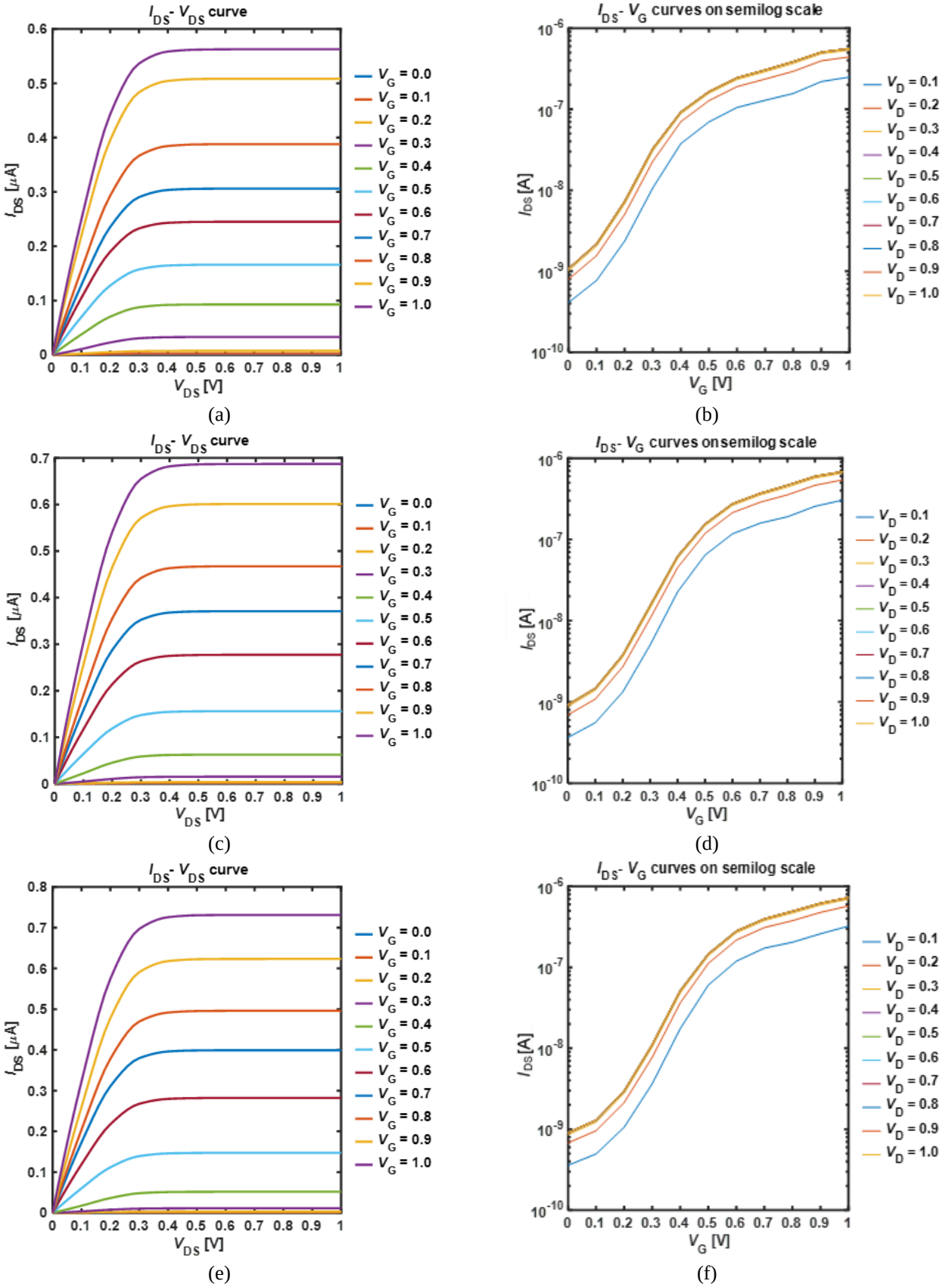

Fig. 7 Drain-source current I_{DS} versus drain-source voltage V_{DS} for n-doped rough-edged 13-AGNRFETs at a doping concentration of (a) 0.02, (c) 0.04 and (e) 0.06 per carbon atom and drain-source current I_{DS} versus gate voltage V_G on a semilogarithmic scale for n-doped rough-edged 13-AGNRFETs at a doping concentration of (a) 0.02, (c) 0.04 and (e) 0.06 per carbon atom

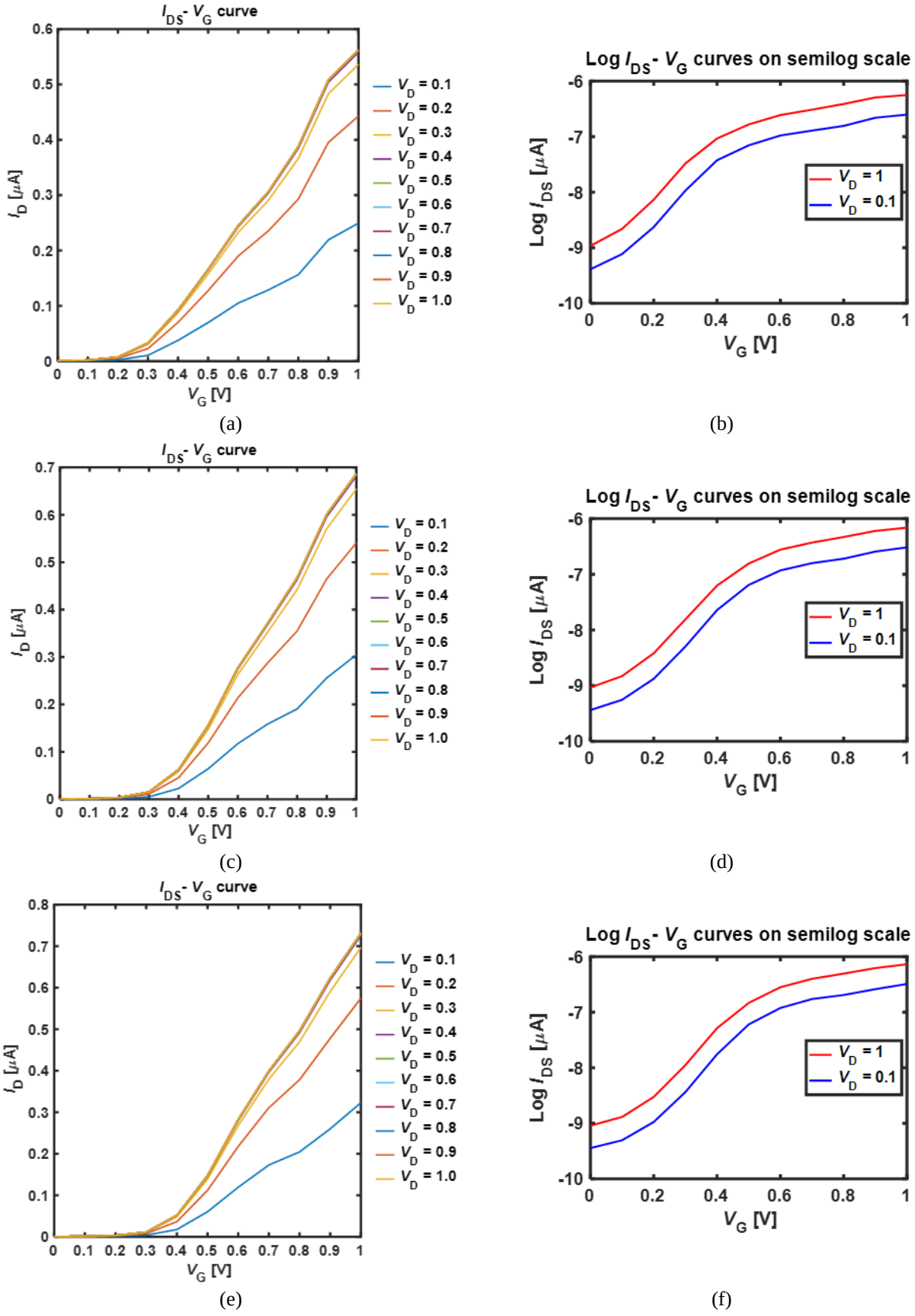

Fig. 8 Drain-source current I_{DS} versus gate voltage V_G for n-doped rough-edged 13-AGNRFETs at a doping concentration of (a) 0.02, (c) 0.04 and (e) 0.06 per carbon atom and the logarithm of drain-source current I_{DS} versus gate voltage V_G on a semilogarithmic scale for n-doped rough-edged 13-AGNRFETs at a doping concentration of (a) 0.02, (c) 0.04 and (e) 0.06 per carbon atom

Table 1 Performance metrics of n-doped rough-edged 13-AGNRFETs at lengths of 5 nm with various doping concentrations

Doping Concentration (per carbon atom)	Subthreshold Swing (mV/dec)	DIBL (mV/V)	On-current I_{ON} (A)	Off-current I_{OFF} (A)	I_{ON}/I_{OFF} ratio	Threshold voltage V_T (V)
0.02	161.48	81.73	5.63×10^{-7}	1.08×10^{-9}	521.30	0.18
0.04	152.19	79.70	6.87×10^{-7}	9.29×10^{-10}	739.50	0.2
0.06	139.44	77.28	7.31×10^{-7}	9.08×10^{-10}	805.07	0.3

5. Conclusions

In conclusion, this work has successfully modelled and simulated the electronic properties of n-doped rough-edged 13-AGNRs at different doping concentration, including the sub-band structure and bandgap; as well as its quantum transport properties at the device level, including the total DOS of the device, transmission coefficient and current-voltage characteristics curves. Numerical real space NNTB approach has been employed to construct the Hamiltonian operator matrix of the simulated nanostructure. Quantum transport properties are simulated via the self-consistent solution of two-dimensional Poisson and Schrödinger equation within the NEGF method. The successive over-relaxation method is coupled with the Poisson equation to speed up the convergence process. Following that, performance metrics of the device including subthreshold swing, drain-induced barrier lowering, on/off current ratio and threshold voltage, are computed. The results of this research show that the bandgap, subthreshold swing and drain-induced barrier lowering are reduced under increasing doping concentration because more carriers are introduced in the nanostructure under higher doping concentration. Therefore, the on-state current is increased for highly-doped rough-edged 13-AGNRFETs and thus higher on/off current ratio. In short, the higher the doping concentration of the channel, the better the gate control of the device. In future work, the effects of channel dopant locations in the AGNRFETs to its device performance could be explored to gain further insights on this interesting bandgap engineering technique.

Acknowledgement

The authors express their deep gratitude for the outstanding support and research-friendly environment offered by Universiti Teknologi Malaysia (UTM). This research received funding from the UTM Fundamental Research (UTMFR) under cost centre number Q.J130000.3823.22H76. The authors also extend their thanks to the Research Management Centre, School of Graduate Studies, and Faculty of Electrical Engineering.

References

Bahrami, S. and Shahhoseini, A. (2017), "The vacancy defect in graphene nano-ribbon field-effect transistor in the presence of an external perpendicular magnetic field", *Microsyst. Technol.*, **23**(2), 321-328. https://doi.org/10.1007/s00542-015-2525-4.

Baildya, N., Ghosh, N.N. and Chattopadhyay, A.P. (2020), "Tailoring electronic and transport properties of edge-terminated armchair graphene by defect formation and N/B doping", *Phys. Lett. A*, **384**(9), 6. https://doi.org/10.1016/j.physleta.2019.126194.

Bouadi, A., Bousahla, A.A., Houari, M.S.A., Heireche, H. and Tounsi, A. (2018), "A new nonlocal HSDT for analysis of stability of single layer graphene sheet", *Adv. Nano Res.*, **6**(2), 147-162. https://doi.org/10.1016/j.physleta.2019.126194.

Cai, J., Pignedoli, C.A., Talirz, L., Ruffieux, P., Söde, H., Liang, L., Meunier, V., Berger, R., Li, R., Feng, X., Müllen, K. and Fasel, R. (2014), "Graphene nanoribbon heterojunctions", *Nature Nanotech.*, **9**(11), 896-900. https://doi.org/10.1038/nnano.2014.184.

Chen, Y.C., Cao, T., Chen, C., Pedramrazi, Z., Haberer, D., de Oteyza, D.G., Fischer, F.R., Louie, S.G. and Crommie, M.F. (2015), "Molecular bandgap engineering of bottom-up synthesized graphene nanoribbon heterojunctions", *Nature Nanotech.*, **10**(2), 156-160. https://doi.org/10.1038/nnano.2014.307.

Chin, H.C., Hamzah, A., Alias, N.E. and Tan, M.L.P. (2023), "Modeling the impact of phonon scattering with strain effects on the electrical properties of MoS2 field-effect transistors", *Micromachines*, **14**(6), 1235. https://doi.org/10.3390/mi14061235.

Chin, H.C., Lim, C.S., Wong, W.S., Danapalasingam, K.A., Arora, V.K. and Tan, M.L.P. (2014), "Enhanced device and circuit-level performance benchmarking of graphene nanoribbon field-effect transistor against a nano-MOSFET with interconnects", *J. Nanomater.*, **2014**(879813), 14. http://doi.org/10.1155/2014/879813.

Dass, D. (2018), "Structural analysis, electronic properties, and band gaps of a graphene nanoribbon: A new 2D materials", *Superlatt. Microstruct.*, **115**, 88-107. https://doi.org/10.1016/j.spmi.2018.01.001.

Datta, S. (1995), *Electronic Transport in Mesoscopic Systems*, Cambridge University Press, Cambridge. https://doi.org/10.1017/CBO9780511805776.

Fiori, G. and Iannaccone, G. (2007), "Simulation of graphene nanoribbon field-effect transistors", *IEEE Electr. Device Lett.*, **28**(8), 760-762. https://doi.org/10.1109/LED.2007.901680.

Fu, H.Y., Sun, F., Liu, R., Suo, Y.Q., Bi, J.J., Wang, C.K. and Li, Z.L. (2019), "Doping-induced giant rectification and negative differential conductance (NDC) behaviors in zigzag graphene nano-ribbon junction", *Phys. Lett. A.* **383**(9), 867-872. https://doi.org/10.1016/j.physleta.2018.12.001.

Gao, R.B., Peng, X.F. and Chen, K.Q. (2018), "Edge-oxidation effects on the thermoelectric properties in graphene nanoribbons", *Physica E*, **104**, 302-308. https://doi.org/10.1016/j.physe.2018.07.038.

Guseinov, N.R., Baigarinova, G.A. and Ilyin, A.M. (2016), "Structural damaging in few-layer graphene due to the low energy electron irradiation", *Adv. Nano Res.*, **4**(1), 45-50. https://doi.org/10.12989/anr.2016.4.1.045.

Huang, B., Yan, Q., Zhou, G., Wu, J., Gu, B.L., Duan, W. and Liu, F. (2007), "Making a field effect transistor on a single graphene

nanoribbon by selective doping", *Appl. Phys. Lett.*, **91**(25), 253122. https://doi.org/10.1063/1.2826547.

Khan, M.I., Buzdar, A.R. and Lin, F. (2014). "Ballistic transport modeling in advanced transistors", *Proceedings of the 2014 12th IEEE International Conference on Solid-State and Integrated Circuit Technology (ICSICT)*, Guilin, China. https://doi.org/10.1109/ICSICT.2014.7021476.

Khorshidsavar, A., Ghoreishi, S.S. and Yousefi, R. (2018), "A computational study of an optimized MOS-like graphene nano ribbon field effect transistor (GNRFET)", *ECS J. Solid State Sci. Technol.*, **7**(3), P96-P101. https://doi.org/10.1149/2.0111803jss.

Lam, K.T., Chin, S.K., Seah, D.W., Kumar, S.B. and Liang, G. (2010), "Effect of ribbon width and doping concentration on device performance of graphene nanoribbon tunneling field-effect transistors", *Japanese J. Appl. Phys.*, **49**(4S), 04DJ10. https://doi.org/10.1143/JJAP.49.04DJ10.

Nazari, A., Faez, R. and Shamloo, H. (2015), "Improving I_{ON}/I_{OFF} and sub-threshold swing in graphene nanoribbon field-effect transistors using single vacancy defects", *Superlatt. Microstruct.*, **86**, 483-492. https://doi.org/10.1016/j.spmi.2015.08.018.

Nazari, A., Faez, R. and Shamloo, H. (2016), "Modeling comparison of graphene nanoribbon field effect transistors with single vacancy defect", *Superlatt. Microstruct.*, **97**, 28-45. https://doi.org/10.1016/j.spmi.2016.06.008.

Nguyen, G.D., Tsai, H.-Z., Omrani, A.A., Marangoni, T., Wu, M., Rizzo, D.J., Rodgers, G.F., Cloke, R.R., Durr, R.A., Sakai, Y., Liou, F., Aikawa, A.S., Chelikowsky, J.R., Louie, S.G., Fischer, F.R. and Crommie, M.F. (2017), "Atomically precise graphene nanoribbon heterojunctions from a single molecular precursor", *Nature Nanotechnol.*, **12**(11), 1077-1082. https://doi.org/10.1038/nnano.2017.155.

Novoselov, K.S., Geim, A.K., Morozov, S., Jiang, D., Zhang, Y., Dubonos, S., Grigorieva, I. and Firsov, A. (2004), "Electric field effect in atomically thin carbon films", *Science*, **306**(5696), 666-669. https://doi.org/10.1126/science.1102896.

Oldiges, P., Vega, R.A., Utomo, H.K., Lanzillo, N.A., Wassick, T., Li, J., Wang, J. and Shahidi, G.G. (2020), "Chip power-frequency scaling in 10/7nm node", *IEEE Access*, **8**, 154329-154337. https://doi.org/10.1109/ACCESS.2020.3017756.

Owlia, H., Keshavarzi, P. and Nasrollahnejad, M.B. (2017), "Effects of Stone-Wales defect position in graphene nanoribbon field-effect transistor", *J. Nano Electr. Phys.*, **9**(6), 06008. https://doi.org/10.21272/jnep.9(6).06008.

Poobalan, P., Wong, Y., Alias, N.E., Isaak, S. and Tan, M.L.P. (2024), "Quantum transport properties of AB bilayer graphene via tight-binding approach with NEGF formalisms", *Appl. Phys. A*, **130**(8), 561. https://doi.org/10.1007/s00339-024-07695-1.

Sampaio-Silva, A., Ferreira, D.F., Silva, C.A.B. and Del Nero, J. (2022), "Hydrogenation, width and strain effect in Me-graphene devices", *Comput. Mater. Sci.*, **210**, 111456. https://doi.org/10.1016/j.commatsci.2022.111456.

Sampaio-Silva, A., Maciel Correa, S., Silva, C.A.B., Jr. and Del Nero, J. (2020), "Electronic transport and its inelastic effects for a doped phagraphene device", *J. Appl. Phys.*, **128**(055104). https://doi.org/10.1063/5.0021492.

Santos, J.C.d.S.d., Ferreira, D.F.S., da Silva, C.A.B. and Del Nero, J. (2020), "Transitions in electrical behavior of Molecular Devices based on 1-D and 2-D graphene-phagraphene-graphene hybrid heterojunctions", *Mater. Chem. Phys.*, **253**, 123420. https://doi.org/10.1016/j.matchemphys.2020.123420.

Shamloo, H., Faez, R. and Nazari, A. (2017), "Performance comparison of ideal and defected bilayer graphene nanoribbon FETs", *Superlatt. Microstruct.*, **111**, 262-272. https://doi.org/10.1016/j.spmi.2017.06.039.

Shamloo, H., Nazari, A., Faez, R. and Shahhoseini, A. (2020), "Local impact of Stone–Wales defect on a single layer GNRFET", *Phys. Lett. A*, **384**(7), 126170. https://doi.org/10.1016/j.physleta.2019.126170.

Son, Y.W., Cohen, M.L. and Louie, S.G. (2006), "Energy gaps in graphene nanoribbons", *Phys. Rev. Lett.*, **97**(21), 216803. https://doi.org/10.1103/PhysRevLett.97.216803.

Tan, M.L.P., Lentaris, G. and Amaratunga, G.A. (2012), "Device and circuit-level performance of carbon nanotube field-effect transistor with benchmarking against a nano-MOSFET", *Nanosc. Res. Lett.*, **7**(1), 467. https://doi.org/10.1186/1556-276X-7-467.

Wong, K.L., Chuan, M.W., Chong, W.K., Alias, N.E., Hamzah, A., Lim, C.S. and Tan, M.L.P. (2019a), "Modeling of low-dimensional pristine and vacancy incorporated graphene nanoribbons using tight binding model and their electronic structures", *Adv. Nano Res.*, **7**(3), 209-221. https://doi.org/10.12989/anr.2019.7.3.209.

Wong, K.L., Chuan, M.W., Hamzah, A., Rusli, S., Alias, N.E., Lim, C.S. and Tan, M.L.P. (2020a), "Carrier statistics of highly doped armchair graphene nanoribbons with edge disorder", *Superlatt. Microstruct.*, **139**, 106404. https://doi.org/10.1016/j.spmi.2020.106404.

Wong, K.L., Chuan, M.W., Hamzah, A., Rusli, S., Alias, N.E., Mohamed Sultan, S., Lim, C.S. and Tan, M.L.P. (2020b), "Carrier transport of rough-edged doped GNRFETs with metal contacts at various channel widths", *Superlatt. Microstruct.*, **143**, 106548. https://doi.org/10.1016/j.spmi.2020.106548.

Wong, K.L., Chuan, M.W., Hamzah, A., Rusli, S., Alias, N.E., Sultan, S.M., Lim, C.S. and Tan, M.L.P. (2020c), "Electronic properties of graphene nanoribbons with line-edge roughness doped with nitrogen and boron", *Physica E*, **117**, 113841. https://doi.org/10.1016/j.physe.2019.113841.

Wong, K.L., Chuan, M.W., Hamzah, A., Rusli, S., Alias, N.E., Sultan, S.M., Lim, C.S. and Tan, M.L.P. (2020d), "Performance metrics of current transport in pristine graphene nanoribbon field effect transistors using recursive non-equilibrium Green's function approach", *Superlatt. Microstruct.*, **145**, 106624. https://doi.org/10.1016/j.spmi.2020.106624.

Wong, K.L., Tan, B.R., Chuan, M.W., Hamzah, A., Rusli, S., Alias, N.E., Sultan, S.M., Lim, C.S. and Tan, M.L.P. (2019b), "Modeling of lightly-doped drain and source contact with boron and nitrogen in graphene nanoribbon", *Chinese J. Phys.*, **62**, 258-273. https://doi.org/10.1016/j.cjph.2019.09.026.

Zenkour, A.M. (2016), "Buckling of a single-layered graphene sheet embedded in visco-Pasternak's medium via nonlocal first-order theory", *Adv. Nano Res.*, **4**(4), 309-326. https://doi.org/10.12989/anr.2016.4.4.309.

CC